Authors' Accepted Manuscript [DOI: 10.1115/1.4056870]
Journal of Mechanisms and Robotics (2023)

Chenhao Lu
Key Laboratory of Concrete and Prestressed Concrete Structures of Ministry of Education, and National Prestress Engineering Research Center, Southeast University, Nanjing 211189, China
e-mail: chenhao_lu@seu.edu.cn

Yao Chen[1]
Key Laboratory of Concrete and Prestressed Concrete Structures of Ministry of Education, and National Prestress Engineering Research Center, Southeast University, Nanjing 211189, China
e-mail: chenyao@seu.edu.cn

Jiayi Yan
Key Laboratory of Concrete and Prestressed Concrete Structures of Ministry of Education, and National Prestress Engineering Research Center, Southeast University, Nanjing 211189, China
e-mail: jyyan_guuru@126.com

Jian Feng
Key Laboratory of Concrete and Prestressed Concrete Structures of Ministry of Education, and National Prestress Engineering Research Center, Southeast University, Nanjing 211189, China
e-mail: fengjian@seu.edu.cn

Pooya Sareh[1]
Creative Design Engineering Lab (Cdel), Department of Mechanical and Aerospace Engineering, School of Engineering, University of Liverpool, Liverpool L69 3GH, UK;
Higher Technical School of Engineering and Industrial Design, Polytechnic University of Madrid (UPM), Ronda de Valencia, 3, Madrid 28012, Spain
e-mail: pooya.sareh@liverpool.ac.uk

Algorithmic Spatial Form-Finding of Four-Fold Origami Structures Based on Mountain-Valley Assignments

Origami has attracted tremendous attention in recent years owing to its capability of inspiring and enabling the design and development of reconfigurable structures and mechanisms for applications in various fields such as robotics and biomedical engineering. The vast majority of origami structures are folded starting from an initial two-dimensional crease pattern. However, in general, the planar configuration of such a crease pattern is in a singular state when the origami starts to fold. Such a singular state results in different motion possibilities of rigid or non-rigid folding. Thus, planar origami patterns cannot act as reliable initial configurations for further kinematic or structural analyses. To avoid the singularities of planar states and achieve reliable structural configurations during folding, we introduce a nonlinear prediction–correction method and present a spatial form-finding algorithm for four-fold origami. In this approach, first, initial nodal displacements are predicted based on the mountain-valley assignments of the given origami pattern, which are applied to vertices to form an initial spatial and defective origami model. Subsequently, corrections of nodal displacements are iteratively performed on the defective model until a satisfactory nonplanar configuration is obtained. Numerical experiments demonstrate the performance of the proposed algorithm in the form-finding of both trivial and non-trivial four-fold origami tessellations. The obtained configurations can be effectively utilized for further kinematic and structural analyses. Additionally, it has been verified that corrected and nonplanar configurations are superior to initial configurations in terms of matrix distribution and structural stiffness.

Keywords: spatial form-finding, flat-foldable origami, kinematic singularity, Miura origami tessellation, rigid-foldability, folding of origami, mechanism design, robot design, theoretical kinematics

1 Introduction

Origami structures possess a range of remarkable properties such as tunable stiffness [1], high strength [2], programmable curvature [3], multistability [4,5], energy absorption [6,7], efficient reconfigurability [8], and negative Poisson's ratio [9–11]. Owing to these desirable characteristics, origami structures have been exploited in a diverse range of applications [12] including deployable structures [13–15], energy absorption structures [16,17], biomedical devices [18], robotics [19,20], and programmable metamaterials [21–23]. As a result, it is crucial for the scientific community to establish effective form-finding theorems that enable designers to find the initial spatial configurations of origami structures for further kinematic and structural analyses.

In recent decades, various studies have been conducted on the methodical design of novel origami patterns [24–27]. To analyze the geometric, kinematic, and mechanical properties of origami structures, Chen et al. [28] introduced graph theory and utilized undirected and directed graph products to represent origami patterns. Moreover, based on the classical theorems and geometric conditions of origami, the graphical method and particle swarm optimization were exploited to develop flat-foldable origami patterns [29,30]. Subsequently, the problem of mountain and valley assignment was solved by mixed-integer linear programming [31,32].

Though various studies [33–36] have focused on origami design, the investigation of kinematic or structural analyses of origami structures has been rather limited. This is because kinematic singularity and motion bifurcation [13] are generally unavoidable in folding problems. Hence, the finite element method has no access to tracking the entire folding of flat-foldable origami from a completely planar state. To facilitate further applications, it is essential to effectively transform planar configurations into spatial ones based on efficient form-finding approaches. Recent studies have demonstrated various approaches to the computational modeling

[1]Corresponding authors.

of different types of origami structures such as scalable [37] and thick rigid-foldable [38] mechanisms.

In the past few decades, some researchers have investigated the rigid folding of single-vertex origami based on spherical trigonometry. For instance, Huffman [39] and Hull [40] developed relationships among the folding angles of crease lines in a single-vertex four-fold origami and established formulas to describe adjacent folding angles of single-vertex origami. Liu et al. [41] proposed a general kinematic model based on four-fold origami. Zimmermann et al. [42] proposed the principle of three units to effectively model the kinematics of degree-n origami vertices. Such findings and methods have also led to the development of theories on multi-vertex origami. Cai et al. [43] investigated the foldability of multi-vertex origami and proved that the Kresling cylinder cannot be rigid-foldable. Wu and You [44] proposed an analytical method to track the entire folding process of multi-vertex origami.

Drawing on the abovementioned studies, various analytical methods have been established to determine the nonplanar configurations of origami structures during folding. For instance, an integral mechanism mode was adopted to accurately follow the motion path of scissor-hinge structures [45]. Moreover, an improved symmetry method for the mobility of kinematically indeterminate pin-jointed structures was proposed by combining graph theory and group theory [46]. Kang et al. [47] introduced a mechanism to accomplish the robust folding of crease patterns via different thermally responsive hydrogels. Based on a bar-and-hinge model, Liu and Paulino [48] proposed an approach for the static and quasi-static analysis of non-rigid origami structures. Jalali et al. [49] introduced the selective hinge removal strategy for the smooth deployment of pin-joint structures with polygonal elements. Chen and Feng [14] proposed a nonlinear prediction–correction algorithm for following the folding behavior of deployable origami structures. However, the algorithm was not able to robustly predict and prevent singular structural configurations in the folding process of the structures.

To overcome the singularity of planar origami, an initial nonplanar configuration is necessary for further kinematic and structural analyses. However, the initial configuration is generally assumed to be known in advance or captured from appropriate geometric/physical models. Hence, in this paper, a nonplanar form-finding algorithm is proposed to accurately obtain the spatial configurations of four-fold origami structures. Section 2 examines the imposition of initial displacements on planar configurations. Subsequently, in terms of geometric and kinematic constraints during folding, nonlinear corrections will be iteratively performed till an allowable accuracy is achieved. Furthermore, to perform robust folding without kinematic singularity, the equivalent pin-jointed model with out-of-plane virtual nodes will be introduced and verified to be superior to the 2D models with crossing virtual members. Numerical examples of four-fold origami structures are presented in Sec. 3 to verify the feasibility, accuracy, and efficiency of the proposed algorithm.

2 Spatial Form-Finding Algorithm

In general, a four-fold origami vertex is considered a single degree-of-freedom (SDOF) system. However, such a vertex is in a singular state when folded from a planar configuration. In other words, each crease might exhibit three different motion states: (i) folded along the expected direction, (ii) folded along the opposite direction, or (iii) remained invariant (no folding). Thus, such a singular state can lead to different rigid or non-rigid motions; therefore, it cannot be utilized as an initial configuration for kinematic or structural analyses. Consequently, it is crucial to carefully track the nonlinear folding of origami structures to obtain reliable spatial configurations. In this section, a nonplanar form-finding approach is proposed to calculate spatial configurations based on a nonlinear prediction–correction algorithm.

2.1 Imposition of Initial Displacements. To track the folding process and obtain initial configurations, it is essential to ensure four-fold origami remains SDOF when it is folded based on hypothetical mountain-valley assignments. To take mountain-valley assignments and expected folding configurations into consideration, appropriate initial displacements should be imposed on each vertex. It ensures each in-plane vertex moves toward the expected direction rather than falling into a singularity. Subsequently, a correction should be applied to the model with initial displacements. Defective models will be corrected to rigid four-fold origami, which is satisfied with the geometrical compatibility conditions via the compatibility matrix. In other words, here, we establish the geometrical incompatibility models of the origami tessellation according to mountain-valley assignments. The edges and creases are defined as

$$x_j = \begin{cases} 1 & \text{if edge or crease } j \text{ is a mountain fold} \\ -1 & \text{if edge or crease } j \text{ is a valley fold} \\ 0 & \text{if edge or crease } j \text{ is a boundary edge} \end{cases} \tag{1}$$

where x_j denotes the initial displacement applied to vertex i by crease j. Equation (1) demonstrates that mountain creases, valley creases, and boundary edges impose $+1$, -1, and 0 displacements on the given vertex, respectively. Especially, symbols + and— denote the positive and negative directions of the z-axis in Fig. 1, respectively. Then, the initial displacement imposed on vertex i can be expressed by

$$u_0(i) = -\eta_j \sum_{j \in E(i)} x_j, \quad i \in V \tag{2}$$

where $E(i) \subseteq E$, $i \in V$ indicates the aggregation of creases connected to vertex i in edges E; E and V respectively denote the assembly of edges and vertices in the crease pattern; and η_j represents the weight coefficient. The aim of adding η_j is to linearly modify the initial displacements of each vertex based on the scales of different origami tessellations.

Figure 1 depicts two different four-fold unit fragments (UFs), adapted from Refs. [24,50,51], as follows: (a) a trivial unit fragment (TUF), and (b) a non-trivial unit fragment (NUF). As can be seen from this figure, TUF contains a trivial flat-foldable vertex M_{T}, whereas NUF contains a no-trivial flat-foldable vertex M_{NT}. The lower part of Fig. 1 illustrates the origami structures with imposed nodal displacements.

2.2 Nonlinear Prediction–Correction Process. Defective models will be produced when each vertex is assigned an initial displacement based on Eqs. (1) and (2). However, it is apparent that deliberately deformed models cannot satisfy the rigid-foldability condition which requires that the lengths of all edges and creases remain unchanged during folding. Therefore, a nonlinear prediction–correction method will be utilized to correct defective models with geometrical incompatibility into rigid origami.

Generally speaking, the displacement compatibility equations of pin-jointed structures are useful for understanding the behavior of origami structures [52,53]. Hence, an equivalent planar pin-jointed model with virtual members will be preferentially adopted to simulate four-fold origami structures. In such a model, crossing virtual members are utilized to replace origami facets to constraint in-plane deformations. Figure 2(a) depicts a typical four-fold origami pattern with four quadrilateral units. Each quadrilateral is defined by four vertices and six members, which include two crossing virtual members. Four quadrilateral units with nine vertices and 20 members form the pin-jointed model for the four-fold origami structure. Specifically, for the modeling of geometrical incompatibility, the deformations of creases and quadrilateral facets can be controlled by predicting and correcting the lengths of members.

The complete displacement compatibility equation of origami structures can be established according to the deformations of members and displacements of nodes during folding. The equation

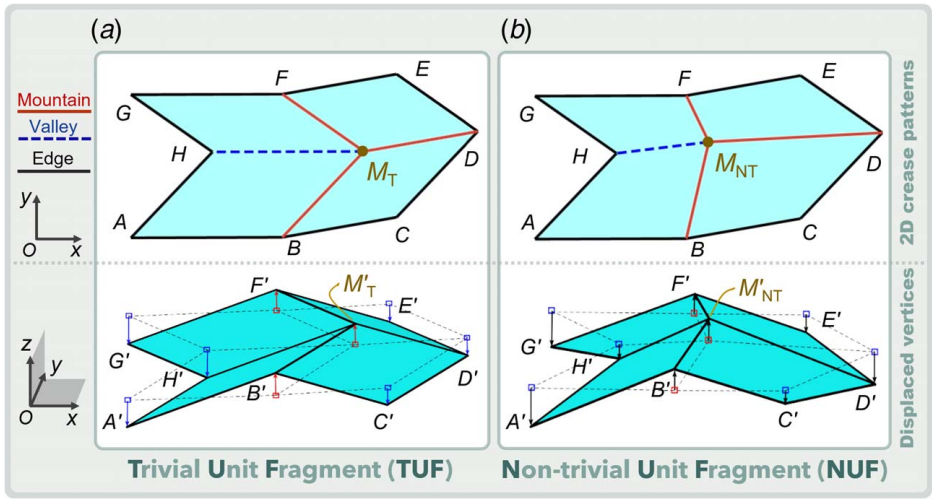

Fig. 1 Two different four-fold unit fragments: (*a*) a trivial unit fragment (TUF) and (*b*) a non-trivial unit fragment (NUF). For each subfigure, the upper part depicts the 2D crease pattern whereas the lower part shows the origami structure with imposed nodal displacements.

is given by

$$\mathbf{J}\mathbf{d} = \mathbf{e} \tag{3}$$

where $\mathbf{J}$ is an $m_0 \times n_0$ compatibility matrix, in which m_0 is the number of independent constraints in the pin-jointed origami model and n_0 is the degree-of-freedom (DOF) of nodes. For instance, the $N_m \times N_n$ pin-jointed model of four-fold origami consists of N_m and N_n basic units in the horizontal and vertical directions, respectively. This model has $(2N_m+1)\times(2N_n+1)$ nodes, $2N_m\times(2N_n+1)+2N_n\times(2N_m+1)$ creases, and $8N_mN_n$ crossing virtual members. When the rigid body constraints are excluded, the number of independent constraints in the pin-jointed model is $m_0 = 2N_m\times(2N_n+1)+2N_n\times(2N_m+1)+8N_mN_n$, and the nodal DOF is $n_0 = 3\times(2N_n+1)\times(2N_m+1)$. In addition, $\mathbf{d}$ denotes a $1\times n_0$ nodal displacement vector, while $\mathbf{e}$ represents an $1\times m_0$ member deformation vector describing the variation of member length in the equivalent pin-jointed structure. The variation can be expressed as

$$\mathbf{e} = \mathbf{l} - \mathbf{l}_0 \tag{4}$$

When the initial displacement $\mathbf{u}_0$ is imposed on the vertices of the planar four-fold origami model, nodal displacement will be

$$\mathbf{d} = \mathbf{u}_0 \tag{5}$$

The displacement of each node consists of two different parts: the real displacement during folding (i.e., $\mathbf{d}_0$) and the pseudo-displacement $\Delta\mathbf{d}$ which needs to be corrected. Typically, origami structures will be folded rigidly when the real displacement $\mathbf{d}_0$ is imposed and the generalized structural deformation $\mathbf{e}$ is zero, i.e.,

$$\mathbf{J}\mathbf{d}_0 = 0 \tag{6}$$

On the other hand, the imposition of pseudo-displacement $\Delta\mathbf{d}$ will generate incompatible deformation $\Delta\mathbf{e}$, i.e.,

$$\mathbf{J}\Delta\mathbf{d} = \Delta\mathbf{e} \tag{7}$$

where $\Delta\mathbf{e}$ is a $1\times m_0$ column vector which represents the deformations of members in the equivalent pin-jointed model. Importantly, incompatible deformations of pin-jointed models will occur due to the existence of $\Delta\mathbf{d}$ when $\mathbf{u}_0$ is imposed; it is necessary to correct deformation $\mathbf{d}$ given by Eq. (5) to obtain the geometric compatible pin-jointed models of rigid origami structures. Then, the corrected

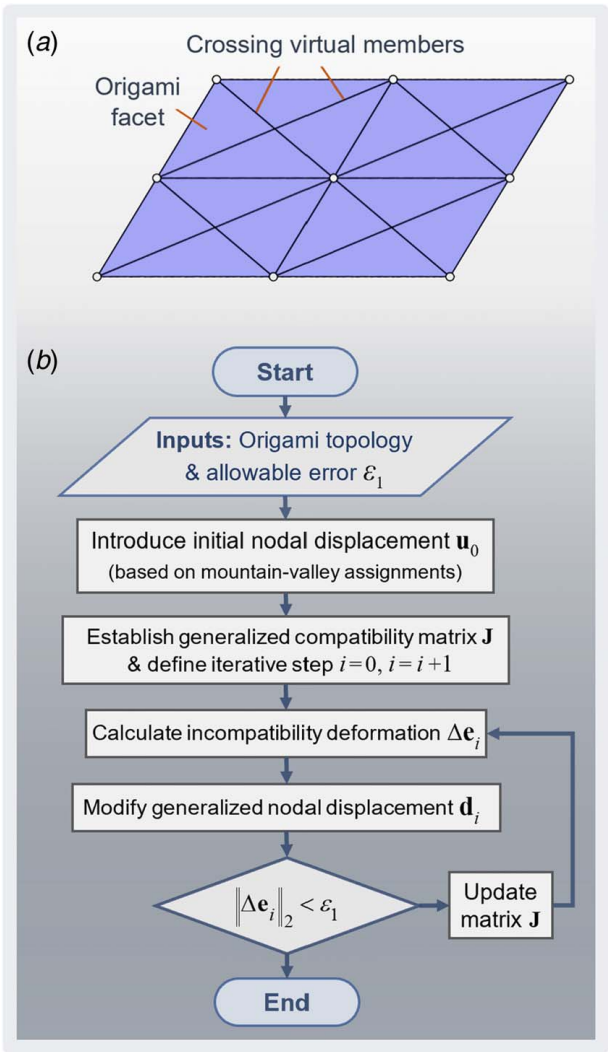

Fig. 2 (*a*) Equivalent planar pin-jointed structure with crossing virtual members for origami facet. (*b*) Flowchart of the form-finding algorithm for four-fold origami based on mountain-valley assignments.

nodal displacement vector $\Delta\mathbf{d}'$ will be given by

$$\Delta\mathbf{d}' = -\mathbf{J}^{+} \cdot \Delta\mathbf{e} \tag{8}$$

where $\mathbf{J}+$ is an $n_0 \times m_0$ matrix which represents the generalized inverse of the compatibility matrix for equivalent pin-jointed structures. The evaluated displacement vector $\Delta\mathbf{d}'$ should be imposed on each node of the pin-jointed structures to correct nodal displacements. As a result, the corrected nodal displacement $\mathbf{d}'$ can be expressed as

$$\mathbf{d}' = \mathbf{d} + \Delta\mathbf{d}' \tag{9}$$

If the origami structure still contains incompatible deformations after the displacement correction, the displacement prediction–correction process based on Eqs. (7)–(9) should be repeated until the generalized deformations of members $\Delta\mathbf{e}$ meet the allowable accuracy; that is

$$\|\Delta\mathbf{e}\|_2 < \varepsilon_1 \tag{10}$$

where $\|\mathbf{A}\|_2$ denotes the two-norm of matrix $\mathbf{A}$, and the allowable accuracy is taken as $\varepsilon_1 = 10^{-10}$ in this study. Then, compatibility matrix $\mathbf{J}$ and incompatible deformation $\Delta\mathbf{e}_i$ can be obtained, and subsequently, the configurations of the origami structure during folding are iteratively updated. Figure 2(*b*) presents the flowchart of this computational procedure, which has been implemented in MATLAB in this study.

2.3 Structural Equivalents of Quadrilateral Facets. Different structural equivalents of the TUF- and NUF-based origami tessellations are, respectively, depicted in Figs. 3(*a*) and 3(*b*), adapted from Ref. [24]. In Figs. 3(*a*,I) and 3(*b*,I), the mountain and valley creases of the origami tessellations are represented by solid and dashed lines, respectively. Based on Eqs. (1) and (2), the initial motion direction of each vertex is designated in Figs. 3(*a*,II) and 3(*b*,II). Due to the periodicity of the patterns, all the vertices can be classified according to the magnitudes and directions of initial displacements. The vertices marked by ⊕ and ⊖ indicate that the corresponding initial displacements should be imposed along the positive and negative z-directions, respectively. In Figs. 3(*a*,III) and 3(*b*,III) based on the equivalent planar pin-jointed model presented in Fig. 2(*a*), the origami facets are replaced by crossing virtual members to constrain in-plane deformations.

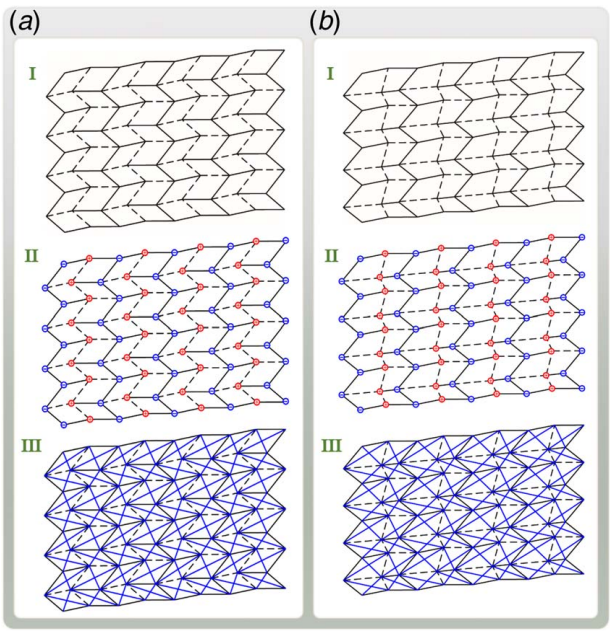

Fig. 3 Different structural representations of (*a*) TUF- and (*b*) NUF-based origami tessellations (adapted from Refs. [24,50]). (I) Mountain-valley assignments of origami crease patterns. (II) Directions of imposed initial displacements. (III) Equivalent planar pin-jointed models.

Based on the mountain-valley assignments, initial displacements are introduced to the vertices when $\eta_j = 0.05L_{\min}$ as illustrated in Figs. 3(*a*,II) and 3(*b*,II), where $L_{\min}$ denotes the minimum length of members. Subsequently, spatial models with incompatible defects will be obtained as depicted in Figs. 4(*a*,I) and 4(*a*,II). To handle these defective models, compatibility matrices will be utilized to correct nodal displacements based on the nonlinear prediction–correction process [13,54,55].

It should be noted that the obtained configurations, shown in Figs. 4(*b*,I) and 4(*b*,II), are in approximately planar states. More specifically, the heights of both structures are no more than $0.05L_{\min}$. Furthermore, the maximum folding angles between adjacent facets ($\rho_{\max}$) during folding are 0.1274 deg and 0.0686 deg, respectively. In other words, by considering the results given in Fig. 4(*b*) as the initial configurations for subsequent kinematic analyses, we cannot avoid kinematic singularities. More importantly, numerical results demonstrate that these configurations cannot satisfy the allowable accuracy using prediction–correction when $\eta_j > 0.2L_{\min}$. Moreover, when $\eta_j = 0.2L_{\min}$, the maximum folding angles are no more than 1 deg.

In conclusion, the obtained configurations based on equivalent planar pin-jointed models neither possess spatial properties nor satisfy the allowable accuracy; therefore, it is crucial to develop a more effective and accurate model for the kinematic analysis of such structures.

To enhance the spatial properties of initial configurations and avoid kinematic singularities and ill-conditioned matrices during kinematic analyses, Zhang et al. [52] added virtual nodes above the planes of origami facets. As shown in Fig. 4(*c*,I), an equivalent spatial pin-jointed model is established based on several out-of-plane virtual nodes and crossing members. Four in-plane nodes and one out-of-plane virtual node are connected by nine rigid members, resulting in a pyramid-shaped three-dimensional structure. Subsequently, the rigid motion is employed to simulate the folding of the origami facet. Concurrently, virtual members are added to origami facets to constrain their deformation. Previous studies [52,56] also illustrate the kinematic simulation of origami with the spatial pin-jointed system in Fig. 4(*c*,II) is superior to that of planar pin-jointed models in Fig. 2(*a*). Furthermore, it prevents generating ill-conditioned matrices which frequently result in incorrect internal mechanism modes and motion paths. Therefore, this study will adopt the equivalent spatial pin-jointed model to carry out numerical experiments.

3 Numerical Experiments

In this section, we present and analyze the spatial form-finding processes of several four-fold origami structures. To obtain accurate spatial configurations, the weight coefficient η_j is set as $0.05L_{\min}$, and the allowable accuracy for incompatible deformations is set as $\varepsilon_1 = 10^{-10}$.

3.1 Form-Finding of a Single Unit Fragment. Equations (11) and (12) represent nodal coordinates vectors $NodeCoord_1$ and $NodeCoord_2$ for TUF and NUF, respectively; these fold patterns, which contain vertices I, II, III,…, IX, are shown in Figs. 5(*a*,i) and 5(*b*,i), respectively

$$NodeCoord_1 = \begin{bmatrix} 2.5 & 0 & 2.5 & 6 & 10.6401 & 8.1401 & 10.6401 & 6 & 5.3176 \\ 5 & 2 & 0 & 0.7 & 0.7128 & 2.7182 & 5.7182 & 5.7 & 2.3134 \end{bmatrix}^T \tag{11}$$

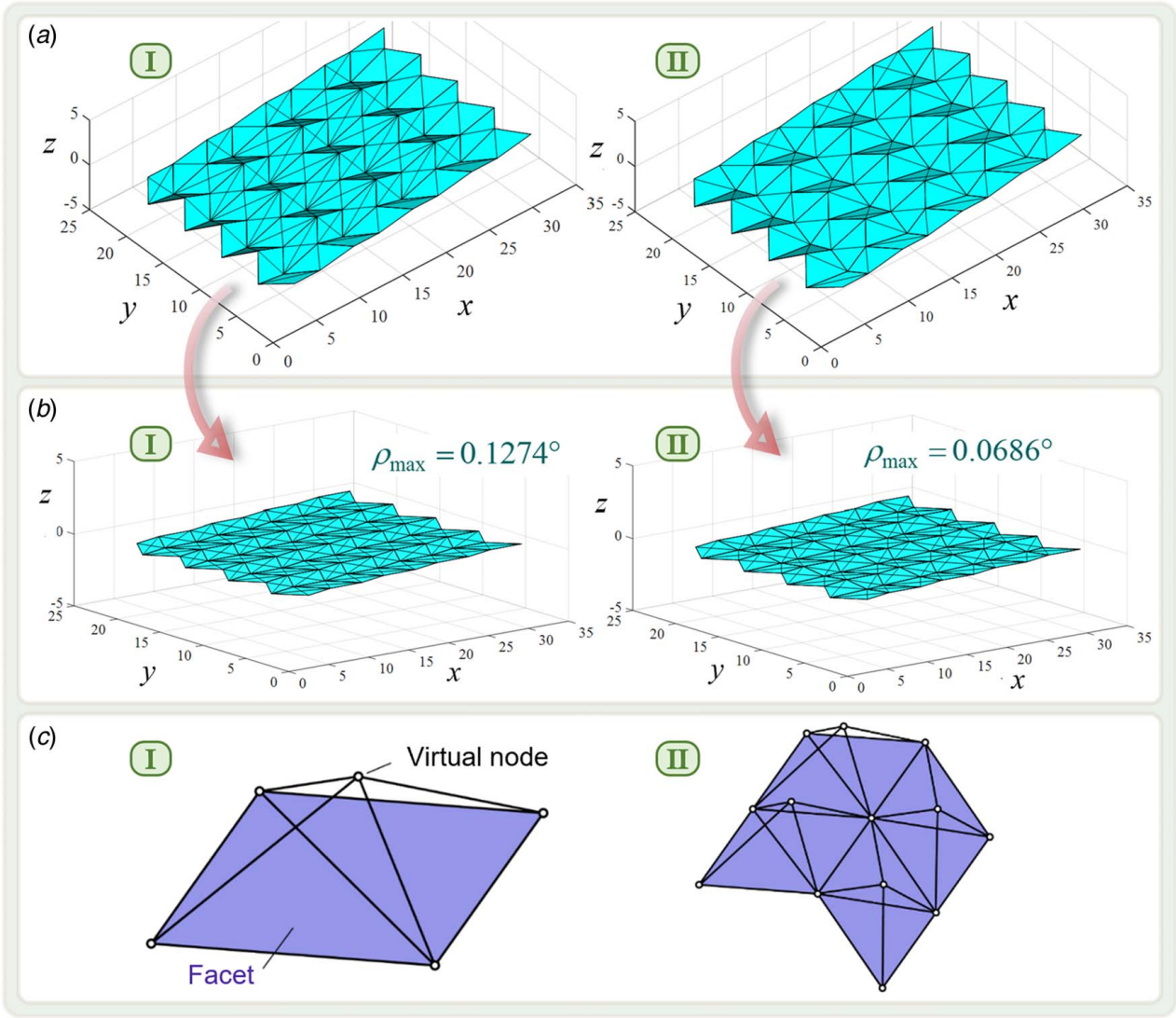

Fig. 4 **(*a*) Defective models obtained from initial displacements based on equivalent planar pin-jointed structures for a (*a*,I) TUF and a (*a*,II) NUF. (*b*) Obtained configurations based on equivalent planar pin-jointed models for the (*b*,I) TUF- and (*b*,II) NUF-based origami tessellations. (c) Equivalent spatial pin-jointed models with out-of-plane virtual nodes: (c,I) a single quadrilateral facet; (c,II) a 2 × 2 four-fold origami pattern.**

$$NodeCoord_2 = \begin{bmatrix} 2.5 & 0 & 2.5 & 6 & 10.6401 & 8.1401 & 10.6401 & 6 & 3.5 \\ 5 & 2 & 0 & 0.7 & 0.7128 & 2.7182 & 5.7182 & 5.7 & 2.7 \end{bmatrix}^T \quad (12)$$

As illustrated in Figs. 5(*a*,i) and 5(*b*,i), the vertices I, II, III, V, VI, and VII have three mountain and one valley creases, marked by (−). On the other hand, the vertices IV, VIII, and IX have three valley and one mountain crease, marked by (+). The directions of initial displacements are according to Figs. 3(*a*,II) and 3(*b*,II). The corresponding spatial pin-jointed models of the patterns presented in Figs. 5(*a*,i) and 5(*b*,i) are depicted in Figs. 5(*a*,ii) and 5(*b*,ii), respectively.

Recall that Fig. 1(*a*) presented earlier provides a comparison between the initial planar state and the deformed state. It is important to mention that, with the prediction of initial displacements, the initial configurations shown by dashed lines gradually transform into the configurations shown by solid lines.

Note that in the defective models, the lengths of members cannot satisfy the constraint conditions. Thus, they are not able to simulate the folding process realistically. Therefore, based on geometric conditions, nonlinear corrections will be repeatedly made to avoid kinematic singularities. To satisfy the allowable accuracy, corrected nodal displacements should ensure that the generalized deformations of the members are appropriately considered.

The nonlinear prediction–correction process starts with the imposition of initial displacements. Subsequently, a compatibility matrix is applied to correct nodal displacements. In this manner, the initially incompatible structure can be gradually transformed into a rigid-foldable origami structure. Figures 6(*a*)–6(*d*), respectively, represent the first, second, third, and fourth corrections for the given TUF. The maximum folding angle between adjacent origami facets during folding ranges from 7.3921 deg to 6.9983 deg with iterations going on. Figure 6(*d*) also provides a visual comparison between the initial (planar) configuration and the final correction of the origami structure. It illustrates that all the vertices can be divided into two groups: (1) a group of vertices moving along the positive direction of the z-axis, and (2) the other vertices moving along the negative direction of the z-axis. In comparison with the initial configuration, the final corrected configuration possesses a spatial geometry; therefore, it will not suffer from kinematic singularity problems in further analyses.

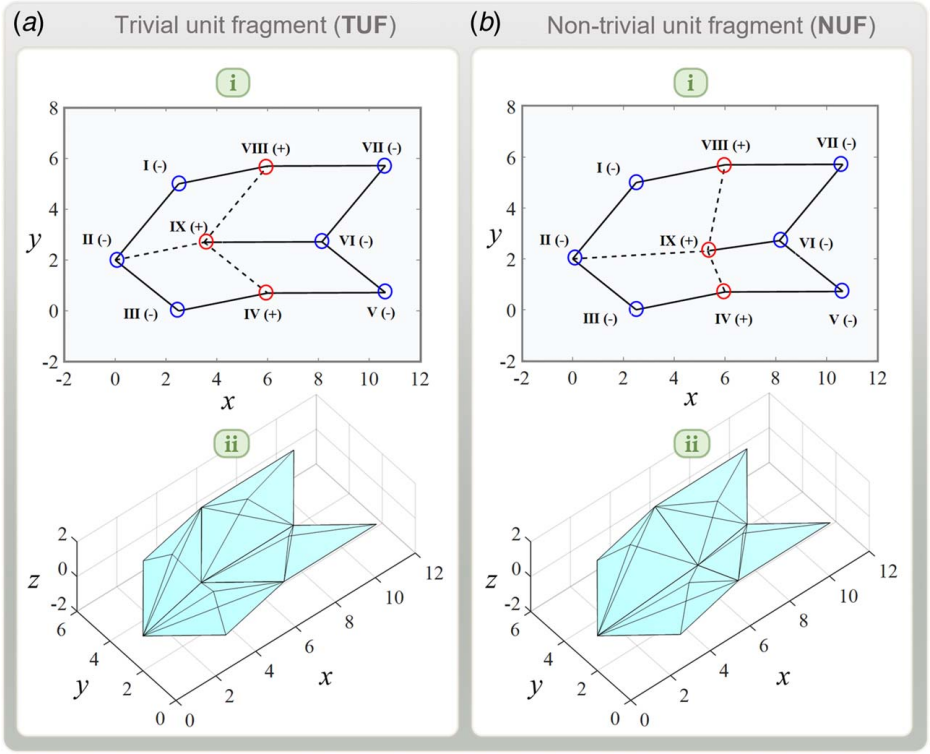

Fig. 5 (*a*,i) and (*b*,i) show crease patterns and predictions of initial nodal displacements for TUF and NUF, respectively. (*a*,ii) and (*b*,ii) depict equivalent spatial pin-jointed models with out-of-plane virtual nodes for TUF and NUF, respectively.

Similarly, with the imposition of initial displacements on the equivalent model for the given NUF, the prediction–correction process involves four iterations. These iterations are shown in Figs. 6(*e*)–6(*h*), which demonstrate that the corrected configurations are spatial structures. Furthermore, the maximum folding angle between adjacent facets during folding varies from 7.2789 deg to 6.6643 deg. Figure 6(*h*) also shows a comparison between the initial (planar) configuration and the final correction. Again, the proposed method avoids kinematic singularities. Moreover, the computation time is less than one second. Therefore, as far as feasibility

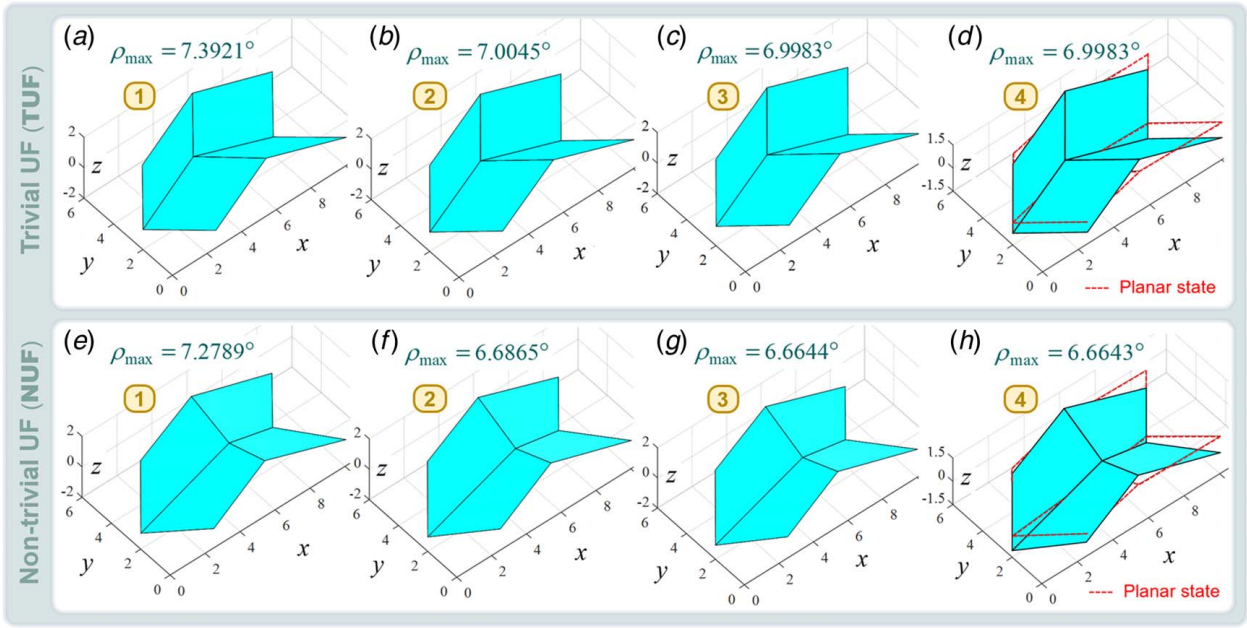

Fig. 6 *Top*: nonlinear prediction–correction process of a given TUF: (*a*) first correction, (*b*) second correction, (c) third correction, (*d*) comparison between the fourth (final) correction and the initial configuration. *Bottom*: nonlinear prediction–correction process of a given NUF: (e) first correction, (*f*) second correction, (*g*) third correction, (*h*) comparison between the fourth (final) correction and the initial configuration.

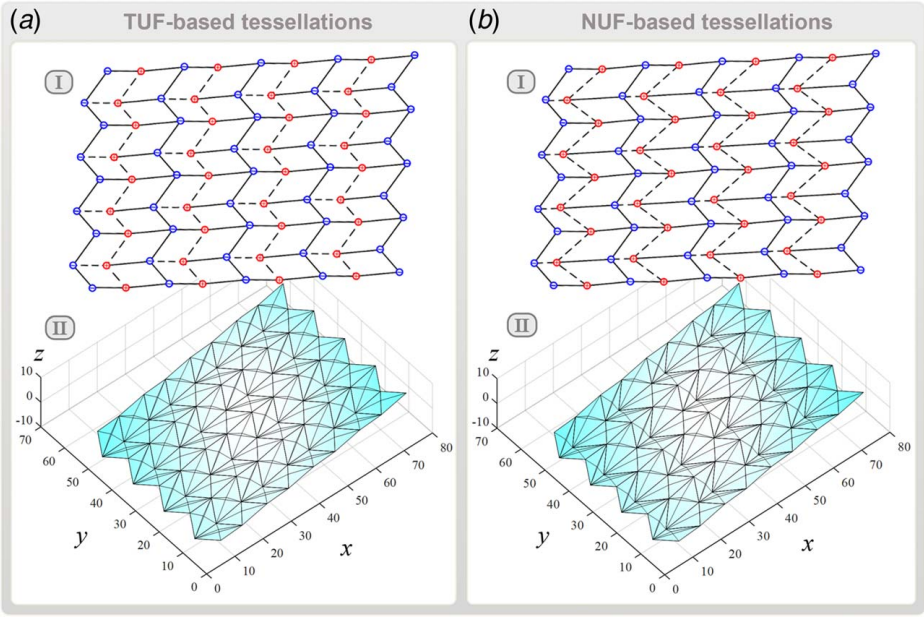

Fig. 7 ***Top*: crease patterns and imposed initial displacements for four-fold tessellations based on (*a*,I) TUF and (*b*,I) NUF. *Bottom*: equivalent spatial models with out-of-plane virtual nodes based on (*a*,II) TUF and (*b*,II) NUF.**

and computational efficiency are concerned, the form-finding process is applicable to such planar configurations.

3.2 Form-Finding and Error Analysis of Tessellations Composed of 4 × 4 UFs. To further examine the feasibility of the proposed form-finding method, some other examples with four-fold origami units are studied in this section. The nodal coordinates vectors for TUF and NUF are presented in Eqs. (13) and (14), respectively. By repeating each unit fragment (UF) four times along the two directions, two 4 × 4 origami tessellations are obtained as shown in Figs. 7(*a*,I) and 7(*b*,I).

According to the proposed form-finding process, the equivalent spatial pin-jointed models with out-of-plane virtual nodes are established and illustrated in Figs. 7(*a*,II) and 7(*b*,II). By introducing the initial displacement vector, it takes four iterations to acquire the final configuration, as shown in Fig. 8. In particular, Figs. 8(*d*) and 8(*h*) present comparisons between their corresponding initial (planar) and final corrected configurations. Compared with initial configurations, the final ones show spatial rigid-foldability, similar to a single UF studied earlier. Moreover, the maximum folding angles between adjacent facets during folding are, respectively, 8.5475 deg and 6.1916 deg. Consequently, the configurations computed by the form-finding process are appropriate as

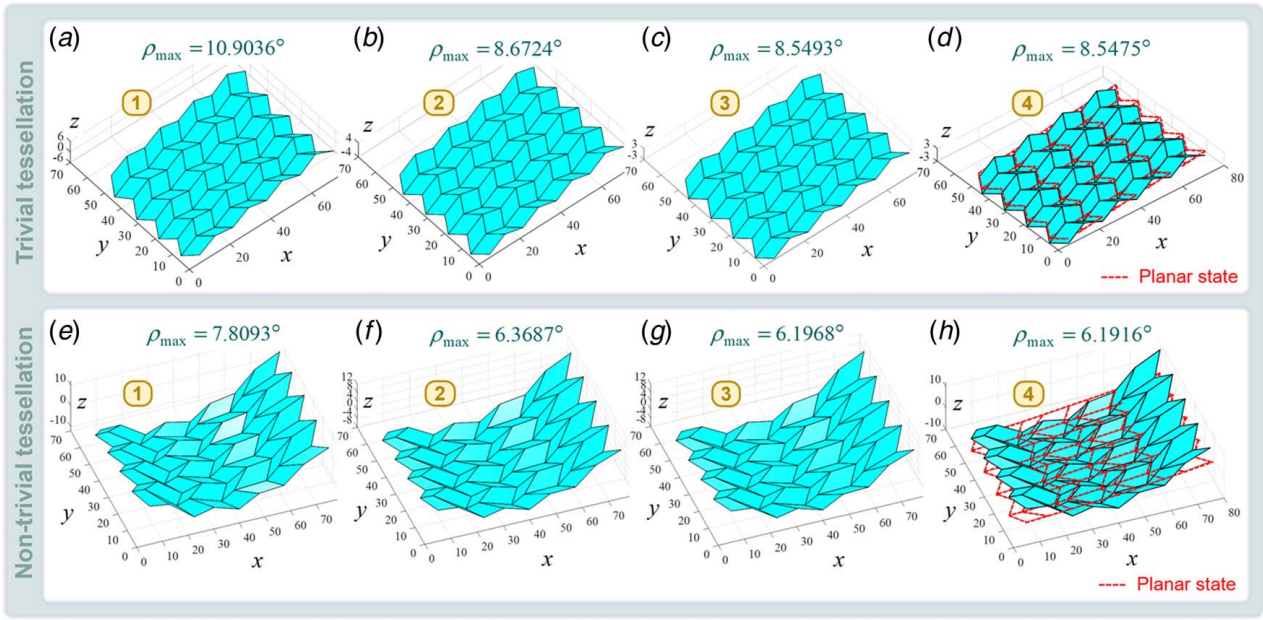

Fig. 8 ***Top*: nonlinear prediction–correction process of a 4 × 4 TUF-based origami tessellation: (*a*) first correction, (*b*) second correction, (*c*) third correction, (*d*) comparison between the fourth (final) correction and the initial configuration. *Bottom*: nonlinear prediction–correction process of a 4 × 4 NUF-based origami tessellation: (*e*) first correction, (*f*) second correction, (*g*) third correction, (*h*) comparison between the fourth (final) correction and the initial configuration.**

Table 1 Errors of the form-finding process for four-fold origami structures

Origami structure	Iterations	Computation time (s)	Coplanar error of origami facet	Error of folding angles
Figures 8(*a*)–(*d*)	4	1.3615	$<10^{-6}$	$<10^{-5}$
Figures 8(*e*)–(*h*)	4	0.6706	$<10^{-6}$	$<10^{-5}$

nonplanar configurations for further kinematic analyses, without being affected by kinematic singularities.

Here, error analysis has been conducted on the configurations obtained from the proposed method. As can be seen from Table 1, the coplanar nodal errors of the individual facets of the final configurations are small enough to be neglected. Furthermore, the obtained origami structure has been verified to be rigidly foldable. Note that the actual folding angles are equal to the theoretical values. Hence, through the geometric compatibility matrix, incompatible configurations can be corrected into ideal nonplanar configurations with comparatively small folding angles.

To investigate the variations of structural stiffness during corrections, comparative studies between planar and corrected configurations are performed. As can be seen from the upper part of Fig. 9, the number of non-zero items of the corrected stiffness matrix is greater than that of the initial stiffness matrix; this implies that the stiffness of the origami structure has been improved by nonlinear corrections. Moreover, we have made a comparison between the initial planar configurations and corrected spatial configurations in terms of the eigenvalue of stiffness matrices. As shown in the lower part of Fig. 9, by comparing the results for corrected spatial configurations with those of initial planar configurations, it can be seen that the minimum eigenvalues of stiffness matrices increase through the prediction–correction process. In other words, the proposed form-finding algorithm is capable of transforming the initial planar configurations into feasible spatial configurations, which can be utilized in further structural analyses without generating ill-conditioned matrices.

3.3 Form-Finding of Origami Structures With Many Vertices and Members. Here, more general examples are presented to further demonstrate the capability of the proposed form-finding approach. According to Secs. 3.1 and 3.2, origami tessellations with much more vertices and members can be obtained by arraying a single UF along both *x*- and *y*- directions. The nodal coordinates vectors of the UFs for the two examined structures are given in Eqs. (13) and (14), respectively.

$$NodeCoord_1 = \begin{bmatrix} 2.5 & 0 & 2.5 & 6 & 9.9262 & 7.4262 & 9.9262 & 6.0000 & 3.4998 \\ 5 & 2 & 0 & 0.7 & 0.7154 & 2.7154 & 5.7154 & 5.7000 & 2.7000 \end{bmatrix}^T \tag{13}$$

$$NodeCoord_2 = \begin{bmatrix} 5 & 0 & 5 & 13 & 23.2798 & 18.2798 & 23.2798 & 13 & 5.1172 \\ 13 & 5 & 0 & 0.5 & 2.2052 & 7.2052 & 15.2052 & 13.5 & 5.5048 \end{bmatrix}^T \tag{14}$$

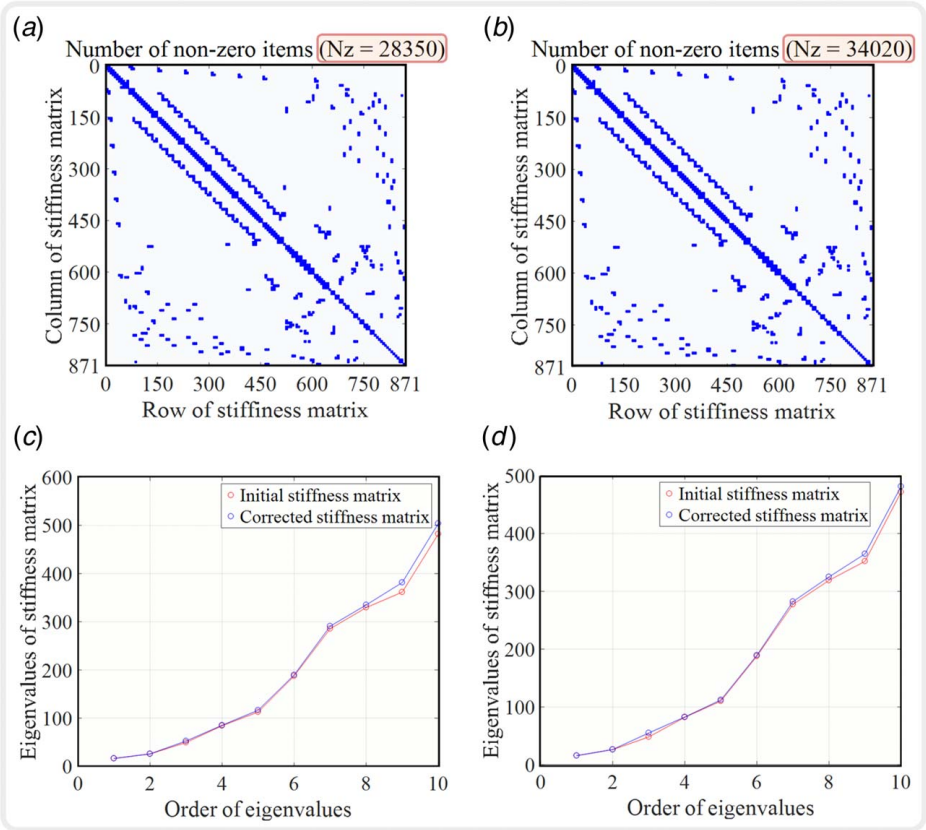

Fig. 9 ***Top*: sparsity pattern of stiffness matrices for the TUF-based origami tessellation: (*a*) initial stiffness matrix, (*b*) corrected stiffness matrix. *Bottom*: comparison between initial planar configurations and corrected spatial configurations in terms of the minimum eigenvalue of stiffness matrices for the 4 × 4 (*c*) TUF-based and (*d*) NUF-based origami tessellations.**

Figure 10 shows spatial pin-jointed models for the 6 × 6 and 8 × 8 origami tessellations, which are respectively based on the vectors in Eqs. (13) and (14). Figure 10(*a*,I) consists of 36 TUFs, while Fig. 10(*a*,II) is composed of 64 NUFs. Similarly, initial displacements will be imposed on each vertex in specific directions. Subsequently, the compatibility matrices will be established to predict and correct structural configurations. Different configurations in Figs. 10(*b*) and 10(*c*) are presented to graphically describe kinematic transformations of complex origami during the nonlinear prediction–correction process.

The TUF-based origami tessellation finishes its form-finding process within 7.1343 s and through four iterations. As illustrated in Fig. 10(*b*), the maximum folding angle between adjacent facets during folding varies between 15.8731 deg and 10.5723 deg. In comparison with the initial planar configuration, the final configuration, shown in Fig. 10(*b*,IV), manifests spatial rigid foldability. In other words, it can be used as an accurate nonplanar configuration for further analysis, without any kinematic singularities.

The NUF-based origami tessellation goes through five iterations in 58.7245 s. Although the computational cost increases, the

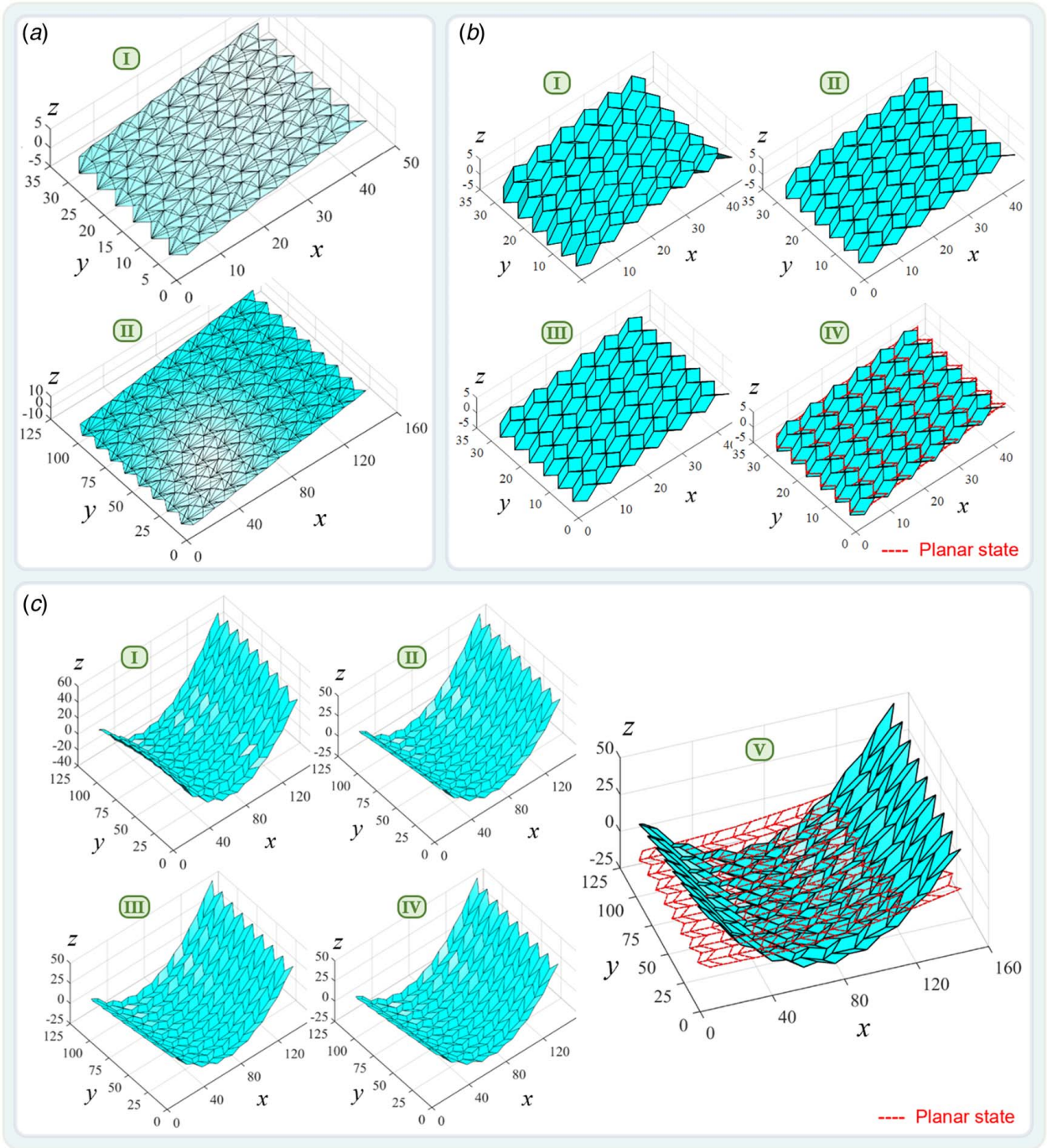

Fig. 10 (*a*) Equivalent spatial models of TUF-based tessellations with out-of-plane virtual nodes: (*I*) a 6 × 6 module; (II) an 8 × 8 module. (*b*) Nonlinear prediction–correction process of a 6 × 6 TUF-based tessellation: (*I*) first correction; (II) second correction; (III) third correction; (IV) comparison between the fourth (final) correction and the initial configuration. (c) Nonlinear prediction–correction process of an 8 × 8 NUF-based tessellation: (*I*) first correction; (II) second correction; (III) third correction; (IV) fourth correction; (*V*) comparison between the fourth (final) correction and the initial configuration.

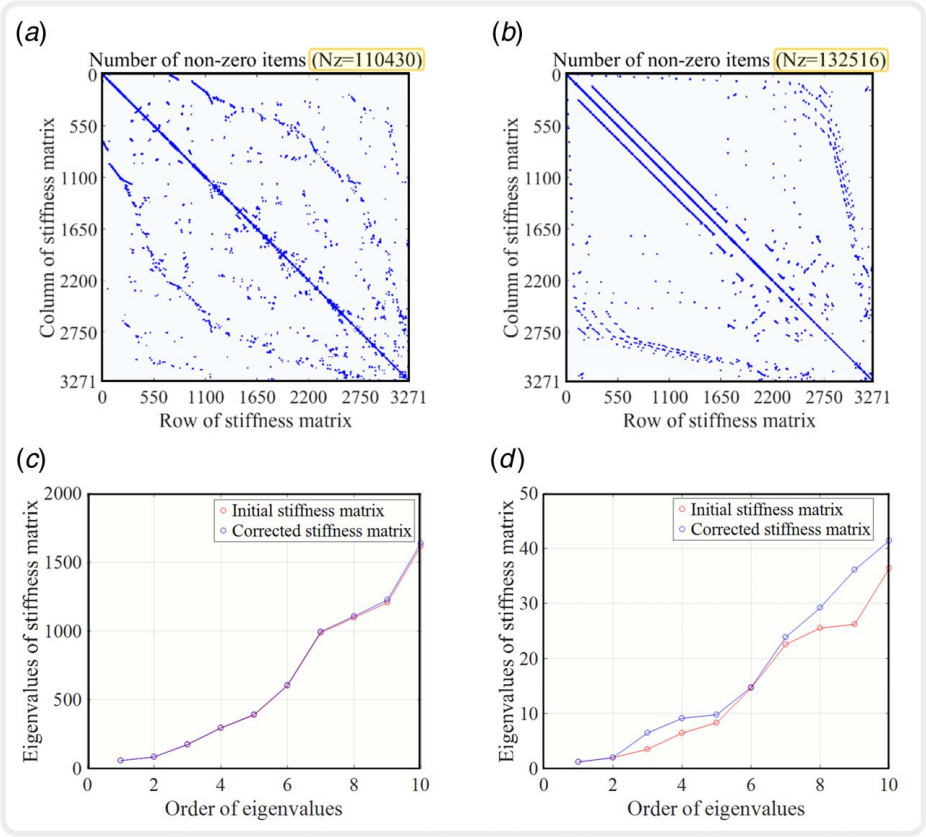

Fig. 11 ***Top*: sparsity pattern of stiffness matrices for the NUF-based origami tessellation: (*a*) initial stiffness matrix and (*b*) corrected stiffness matrix. *Bottom*: comparison between initial planar configurations and corrected spatial configurations in terms of the minimum eigenvalue of stiffness matrices for (*c*) the 6 × 6 TUF-based origami tessellation and (*d*) the 8 × 8 NUF-based origami tessellation.**

terminal configuration satisfies allowable accuracy and exhibits spatial characteristics. Note that this generalized four-fold crease pattern retains the lowest order of 2D symmetry [24,57]. The initial displacement will comparatively cause significant deformation. The maximum folding angle between adjacent facets during folding gradually decreases to 6.0205 deg. In summary, it demonstrates that the proposed form-finding algorithm is applicable to both TUF- and NUF-based origami tessellations.

With the correction process going on, it is necessary to study the transformation of stiffness matrices for planar and spatial configurations. As can be seen from Figs. 11(*a*) and 11(*b*), the corrected stiffness matrix has more non-zero items than the initial stiffness matrix. In other words, there is an improvement in the original ill-conditioned stiffness matrices. Figures 11(*c*) and 11(*d*) demonstrate the minimum eigenvalues of the stiffness matrices; improvements can be seen in both 6 × 6 TUF- and 8 × 8 NUF-based origami tessellations in terms of the lower modes of eigenvalues. Given spatial characteristics and improvements in stiffness matrices, such nonplanar configurations are suitable to be utilized as initial configurations for further analyses.

4 Conclusions

In this study, we developed a nonplanar form-finding algorithm for four-fold origami which enables us to accurately calculate spatial configurations from a completely planar state. The obtained configurations are of particular importance for overcoming kinematic singularities or ill-conditioned matrices in structural and kinematic analyses. Initial displacements have been predicted and imposed on each vertex to generate a defective origami model according to mountain and valley assignments. Subsequently, virtual nodes were introduced to generate equivalent spatial models. Finally, nodal displacements are corrected iteratively as long as the accuracy is allowable.

With the presentation and discussion of numerical experiments, the proposed approach has been verified to be effective in obtaining compatible configurations, as well as origami structures with many vertices and considerable irregularity. Notably, in comparison with the defective planar model, the defective spatial model is a better approach to obtaining nonplanar configurations because it needs much fewer iterations and has higher accuracy. Error analyses illustrated that the corrected configurations satisfied the requirements of flat foldability. Moreover, it was shown that stiffness is improved during nonlinear corrections. Future studies will focus on the application of this algorithm to complex origami patterns with arbitrary mountain-valley assignments.

Acknowledgment

This work was supported by the National Natural Science Foundation of China (Grants Nos. 51978150 and 52050410334), the Southeast University "Zhongying Young Scholars" project, and the Fundamental Research Funds for the Central Universities. The authors are grateful to the editors and anonymous reviewers for their useful comments and suggestions which led to the improvement of the paper.

Conflict of Interest

There are no conflicts of interest.

Data Availability Statement

The authors attest that all data for this study are included in the paper.

Nomenclature

i = A typical vertex of the basic unit in the origami model
$\mathbf{d}$ = Nodal displacement vector
$\mathbf{e}$ = Member deformation vector
E = Assembly of edges in the crease pattern
V = Assembly of vertices in the crease pattern
$\mathbf{J}$ = Compatibility matrix
$\mathbf{l}$ = Initial length of members
m_0 = Number of independent constraints in the pin-jointed origami model
n_0 = degree-of-freedom of nodes
x_j = Initial displacement applied to vertex i by crease j
$\mathbf{d}_0$ = Real displacement during folding
$L_{\min}$ = Minimum length of members
$\mathbf{l}_0$ = Length of members after deformation
$\mathbf{d}'$ = Corrected nodal displacement
$\mathbf{J}^+$ = generalized inverse of compatibility matrix
$\mathbf{u}_0(i)$ = initial displacement imposed on vertex i
$\Delta\mathbf{d}$ = pseudo-displacement
$\Delta\mathbf{d}'$ = evaluated displacement vector
$\Delta\mathbf{e}$ = incompatible deformation
η_j = weight coefficient of initial displacement
$\|*\|_2$ = 2-norm of a matrix *
DOF = degree-of-freedom
NUF = non-trivial unit fragment
SDOF = single degree-of-freedom
TUF = trivial unit fragment
UF = unit fragment

References

[1] Ma, J., Song, J., and Chen, Y., 2018, "An Origami-Inspired Structure With Graded Stiffness," Int. J. Mech. Sci., **136**, pp. 134–142.
[2] Qiu, C., Zhang, K., and Dai, J. S., 2016, "Repelling-Screw Based Force Analysis of Origami Mechanisms," ASME J. Mech. Rob., **8**(3), p. 031001.
[3] Sareh, P., and Guest, S. D., 2015, "Designing Symmetric Derivatives of the Miura-ori," *Advances in Architectural Geometry 2014*, Springer, Cham, pp. 233–241.
[4] Wang, L. C., Song, W. L., Zhang, Y. J., Qu, M. J., Zhao, Z., Chen, M., Yang, Y., Chen, H., and Fang, D., 2020, "Active Reconfigurable Tristable Square-Twist Origami," Adv. Funct. Mater., **30**(13), p. 1909087.
[5] Zhang, K. T., Fang, Y. F., Fang, H. R., and Dai, J. S., 2010, "Geometry and Constraint Analysis of the Three-Spherical Kinematic Chain Based Parallel Mechanism," ASME J. Mech. Rob., **2**(3), p. 031014.
[6] Sareh, P., Chermprayong, P., Emmanuelli, M., Nadeem, H., and Kovac, M., 2018, "The Spinning Cyclic 'Miura-ORing'for Mechanical Collision-Resilience," Origami, **7**(3), pp. 981–994.
[7] Gao, G., Zhuo, T., and Guan, W., 2020, "Recent Research Development of Energy-Absorption Structure and Application for Railway Vehicles," J. Cent. South Univ., **27**(4), pp. 1012–1038.
[8] Liu, S., Yang, Q., and Tao, R., 2020, "Four-Dimensional Printed Self-Deploying Circular Structures With Large Folding Ratio Inspired by Origami," J. Intell. Mater. Syst. Struct., **31**(18), pp. 2128–2136.
[9] You, Z., 2014, "Folding Structures Out of Flat Materials," Science, **345**(6197), pp. 623–624.
[10] Yasuda, H., and Yang, J., 2015, "Reentrant Origami-Based Metamaterials with Negative Poisson's Ratio and Bistability," Phys. Rev. Lett., **114**(18), p. 185502.
[11] Pratapa, P. P., Liu, K., and Paulino, G. H., 2019, "Geometric Mechanics of Origami Patterns Exhibiting Poisson's Ratio Switch by Breaking Mountain and Valley Assignment," Phys. Rev. Lett., **122**(15), p. 155501.
[12] Fan, W., Chen, Y., Li, J., Sun, Y., Feng, J., Hassanin, H., and Sareh, P., 2021, "Machine Learning Applied to the Design and Inspection of Reinforced Concrete Bridges: Resilient Methods and Emerging Applications," Structures, **33**, pp. 3954–3963.
[13] Chen, Y., Feng, J., and Sun, Q., 2018, "Lower-Order Symmetric Mechanism Modes and Bifurcation Behavior of Deployable Bar Structures With Cyclic Symmetry," Int. J. Solids Struct., **139–140**, pp. 1–14.
[14] Chen, Y., and Feng, J., 2013, "Folding of a Type of Deployable Origami Structures," Int. J. Struct. Stab. Dyn., **12**(06), p. 1250054.
[15] Sareh, P., and Guest, S. D., 2015, "A Framework for the Symmetric Generalisation of the Miura-ori," Int. J. Space Struct., **30**(2), pp. 141–152.
[16] Sareh, P., Chermprayong, P., Emmanuelli, M., Nadeem, H., and Kovac, M., 2018, "Rotorigami: A Rotary Origami Protective System for Robotic Rotorcraft," Sci. Rob., **3**(22), p. eaah5228.
[17] Wang, Z., Shi, C., Ding, S., and Liang, X., 2020, "Crashworthiness of Innovative Hexagonal Honeycomb-Like Structures Subjected to Out-of-Plane Compression," J. Cent. South Univ., **27**(2), pp. 621–628.
[18] Pinson, M. B., Stern, M., Carruthers Ferrero, A., Witten, T. A., Chen, E., and Murugan, A., 2017, "Self-Folding Origami at Any Energy Scale," Nat. Commun., **8**(1), pp. 1–8.
[19] Zhang, K. T., Qiu, C., and Dai, J. S., 2016, "An Extensible Continuum Robot With Integrated Origami Parallel Modules," ASME J. Mech. Rob., **8**(3), p. 031010.
[20] Dai, J. S., and Caldwell, D. G., 2010, "Origami-Based Robotic Paper-and-Board Packaging for Food Industry," Trends Food Sci. Technol., **21**(3), pp. 153–157.
[21] Fang, H., Chu, S. C. A., Xia, Y., and Wang, K. W., 2018, "Programmable Self-Locking Origami Mechanical Metamaterials," Adv. Mater., **30**(15), p. 1706311.
[22] Zhai, Z., Wang, Y., and Jiang, H., 2018, "Origami-Inspired, On-Demand Deployable and Collapsible Mechanical Metamaterials With Tunable Stiffness," Proc. Natl. Acad. Sci., **115**(9), pp. 2032–2037.
[23] Sun, Y., Ye, W., Chen, Y., Fan, W., Feng, J., and Sareh, P., 2021, "Geometric Design Classification of Kirigami-Inspired Metastructures and Metamaterials," Structures, **33**, pp. 3633–3643.
[24] Sareh, P., 2019, "The Least Symmetric Crystallographic Derivative of the Developable Double Corrugation Surface: Computational Design Using Underlying Conic and Cubic Curves," Mater. Des., **183**, p. 108128.
[25] McAdams, D. A., and Li, W., 2014, "A Novel Method to Design and Optimize Flat-Foldable Origami Structures Through a Genetic Algorithm," ASME J. Comput. Inf. Sci. Eng., **14**(3), p. 031008.
[26] Chen, Y., Yan, J., and Feng, J., 2019, "Geometric and Kinematic Analyses and Novel Characteristics of Origami-Inspired Structures," Symmetry, **11**(9), p. 1101.
[27] Sareh, P., and Chen, Y., 2020, "Intrinsic non-Flat-Foldability of Two-Tile DDC Surfaces Composed of Glide-Reflected Irregular Quadrilaterals," Int. J. Mech. Sci., **185**, p. 105881.
[28] Chen, Y., Sareh, P., Yan, J., Fallah, A. S., and Feng, J., 2019, "An Integrated Geometric-Graph-Theoretic Approach to Representing Origami Structures and Their Corresponding Truss Frameworks," ASME J. Mech. Des., **141**(9), p. 091402.
[29] Yan, J., Li, J., Chen, Y., and Feng, J., 2021, "Developing Novel Patterns for six-Fold Origami Structures Using Graph Theory and Optimization Algorithms," J. Build. Struct., **43**(09), pp. 277–285.
[30] Chen, Y., Yan, J., Feng, J., and Sareh, P., 2021, "Particle Swarm Optimization-Based Metaheuristic Design Generation of Non-Trivial Flat-Foldable Origami Tessellations With Degree-4 Vertices," ASME J. Mech. Des., **143**(1), p. 011703.
[31] Chen, Y., Fan, L., Bai, Y., Feng, J., and Sareh, P., 2020, "Assigning Mountain-Valley Fold Lines of Flat-Foldable Origami Patterns Based on Graph Theory and Mixed-Integer Linear Programming," Comput. Struct., **239**, p. 106328.
[32] Li, J., Chen, Y., Feng, X., Feng, J., and Sareh, P., 2021, "Computational Modeling and Energy Absorption Behavior of Thin-Walled Tubes With the Kresling Origami Pattern," J. Int. Assoc. Shell Spatial Struct., **62**(2), pp. 71–81.
[33] Sareh, P., and Guest, S. D., 2015, "Design of Isomorphic Symmetric Descendants of the Miura-Ori," Smart Materials and Structures, **24**(8), p. 085001.
[34] Sareh, P., and Guest, S. D., 2015, "Design of non-Isomorphic Symmetric Descendants of the Miura-ori," Smart Materials and Structures, **24**(8), p. 085002.
[35] Nojima, T., 2002, "Modelling of Folding Patterns in Flat Membranes and Cylinders by Origami," JSME Int. J., Ser. C, **45**(1), pp. 364–370.
[36] Chen, Y., Lu, C., Yan, J., Feng, J., and Sareh, P., 2022, "Intelligent Computational Design of Scalene-Faceted Flat-Foldable Tessellations," J. Comput. Des. Eng., **9**(5), pp. 1765–1774.
[37] Filipov, E. T., Liu, K., Tachi, T., Schenk, M., and Paulino, G. H., 2017, "Bar and Hinge Models for Scalable Analysis of Origami," Int. J. Solids Struct., **124**, pp. 26–45.
[38] Lang, R. J., Nelson, T., Magleby, S., and Howell, L., 2017, "Thick Rigidly Foldable Origami Mechanisms Based on Synchronized Offset Rolling Contact Elements," ASME J. Mech. Rob., **9**(2), p. 021013.
[39] Huffman, D. A., 1976, "Curvature and Creases: A Primer on Paper," IEEE Trans. Comput., **C-25**(10), pp. 1010–1019.
[40] Hull, T., 2012, *Project Origami: Activities for Exploring Mathematics*, CRC Press, Boca Raton London New York.
[41] Liu, S., Lv, W., Chen, Y., and Lu, G., 2016, "Deployable Prismatic Structures with Rigid Origami Patterns," ASME J. Mech. Rob., **8**(3), p. 031002.
[42] Zimmermann, L., Shea, K., and Stanković, T., 2020, "Conditions for Rigid and Flat Foldability of Degree-n Vertices in Origami," ASME J. Mech. Rob., **12**(1), p. 011020.
[43] Cai, J., Liu, Y., Ma, R., Feng, J., and Zhou, Y., 2017, "Nonrigidly Foldability Analysis of Kresling Cylindrical Origami," ASME J. Mech. Rob., **9**(4), p. 041018.
[44] Wu, W., and You, Z., 2010, "Modelling Rigid Origami With Quaternions and Dual Quaternions," Proc. R. Soc. A, **466**(2119), pp. 2155–2174.
[45] Chen, Y., Fan, L., and Feng, J., 2017, "Kinematic of Symmetric Deployable Scissor-Hinge Structures With Integral Mechanism Mode," Comput. Struct., **191**, pp. 140–152.

[46] Chen, Y., and Feng, J., 2016, "Improved Symmetry Method for the Mobility of Regular Structures Using Graph Products," J. Struct. Eng., **142**(9), p. 04016051.
[47] Kang, J. H., Kim, H., Santangelo, C. D., and Hayward, R. C., 2019, "Enabling Robust Self-Folding Origami by Pre-Biasing Vertex Buckling Direction," Adv. Mater., **31**(39), p. 0193006.
[48] Liu, K., and Paulino, G. H., 2017, "Nonlinear Mechanics of Non-Rigid Origami: an Efficient Computational Approach," Proc. R. Soc. A, **473**(2206), pp. 1–28.
[49] Jalali, E., Soltanizadeh, H., Chen, Y., Xie, Y. M., and Sareh, P., 2022, "Selective Hinge Removal Strategy for Architecting Hierarchical Auxetic Metamaterials," Commun. Mater., **3**(1), pp. 1–15.
[50] Sareh, P., 2014, *Symmetric Descendants of the Miura-ori*, PhD dissertation, University of Cambridge, Cambridge, UK.
[51] Sareh, P., and Guest, S. D., 2012, "Tessellating Variations on the Miura Fold Pattern," Proceedings of the IASS-APCS Symposium, Seoul, South Korea, Vol. 21, pp. 1070–1078.
[52] Zhang, T., Kawaguchi, K., and Wu, M., 2018, "A Folding Analysis Method for Origami Based on the Frame With Kinematic Indeterminacy," Int. J. Mech. Sci., **146**, pp. 234–248.
[53] Li, Y., 2020, "Motion Paths Finding for Multi-Degree-of-Freedom Mechanisms," Int. J. Mech. Sci., **185**, p. 105709.
[54] Chen, Y., Feng, J., and Zhang, Y., 2014, "A Necessary Condition for Stability of Kinematically Indeterminate Pin-Jointed Structures With Symmetry," Mech. Res. Commun., **60**, pp. 64–73.
[55] Chen, Y., Guest, S. D., Fowler, P. W., and Feng, J., 2012, "Two-Orbit Switch-Pitch Structures," J. Int. Assoc. Shell Spatial Struct., **53**(3), pp. 157–162.
[56] Zhang, T., and Kawaguchi, K. I., 2021, "Folding Analysis for Thick Origami with Kinematic Frame Models Concerning Gravity," Autom. Constr., **127**, p. 103691.
[57] Zhang, P., Fan, W., Chen, Y., Feng, J., and Sareh, P., 2022, "Structural Symmetry Recognition in Planar Structures Using Convolutional Neural Networks," Eng. Struct., **260**, p. 114227.